Synthesis of Hierarchical Graphene Coated Porous Si Anode for Lithium-Ion Batteries

Shuai Xu,[a] Jigang Zhou,[b] Lucia Zuin,[b] Di Sun,[c] Julia Zhao,[c] Abdelmalek Bellal,[a] and Xiaodong Hou[*,a]

[a] College of Engineering and Mine, University of North Dakota, Grand Forks, North Dakota, 58202, United States

[b] Canadian Light Source Inc., Saskatoon, S7N 2V3, Canada

[c] Department of Chemistry, University of North Dakota, Grand Forks, North Dakota, 58202, United States

[*] Corresponding author. Email address: xiaodong.hou@und.edu

ABSTRACT: The ultra-high capacity and widespread availability of Si materials have resulted in them being the focus of extensive studies to replace the graphite anode. However, the main barriers preventing the Si anodes from large-scale applications are their huge volume change and severe interface reactions in the lithiation/delithiation process, which pulverizes its structure and subsequently deteriorates its cycle life. Here, micrometer-scale porous Si coated with graphene coating (mpSi@G) has been synthesized by using SiO_2 nanoparticles and novel coal-derived humic acid as feedstocks through a magnesiothermic reduction, followed by spray drying and calcination techniques. SEM, Raman, and X-ray absorption analysis demonstrate that the hierarchical graphene shell and micrometer-sized porous Si structure effectively release the Si anode's mechanical stress upon lithiation to achieve good structural stability. The synthesized mpSi@G anode delivers a high initial lithiation capacity of 2974.9 mAh g^{-1} at 0.1 A g^{-1} with an initial coulombic efficiency of 70.2%. Furthermore, the conductive hierarchical graphene network, along with the tight contacts of porous-Si and the graphene shell, contribute to a high capacity of 1109.5 mAh g^{-1} at a high current density of 5.0 A g^{-1}, showing excellent rate capability.

KEYWORDS: lithium-ion battery, silicon, humic acid, hierarchical structure, magnesiothermic reduction

1.   Introduction

Future lithium-ion battery (LIB) anodes must meet the demand for high energy density to be sufficient for electronic and energy storage systems [1-3]. With a theoretical capacity of over 4000 mAh g^{-1}, silicon (Si) offers over ten times the capacity of the commonly used graphite anode, making it a promising candidate to replace graphite. Besides, silicon resources are widely available and abundant, thus reinforcing their ideality of being used to meet the skyrocketing development of the LIB anode market [4]. However, the significant drawback of Si is its considerable volume expansion and shrinkage upon charge/discharge cycling (~ 400%), which pulverizes Si particles and subsequently makes the Si particles lose electrical contact with current collectors [5, 6]. Furthermore, Si and the electrolytes undergo a reaction, resulting in the growth of a solid-electrolyte interface (SEI) which is unceasing in subsequent cycles. This continual SEI formation consumes electrolytes, resulting in the thickening of the SEI and compromised Li$^+$ transport. The combination of these factors ultimately results in low cycling efficiency and capacity loss.

So far, plenty of approaches have been proposed to address the above problems. Among them, making nanosized silicon (nano-Si) Si is widely considered to be one of the most effective solutions, as nano-Si ($D < 150$ nm) has been demonstrated to survive cycling without pulverization [7, 8]. Nano-Si also decreases the diffusion length for lithium ions [9-11]. Based on this, numerous types of nanowires [12], nanotubes [13, 14], and nanospheres [15] have been synthesized and demonstrated to improve battery performance. Nevertheless, these nano-Si structures are accompanied by enlarged surface areas, which intensify the SEI formation between Si and electrolytes. Moreover, the synthesis of nano-Si requires complicated processes, making nano-Si very expensive and impractical for large-scale production [4]. Compared to nano-silicon, micrometer-sized porous silicon, which is taken as clusters of many nano-Si particles and voids, has some unique advantages: smaller surface area, much lower viscosity, and better thermodynamic stability [6, 16]. The voids in the porous structure accommodate silicon expansion and contraction freely during the lithiation/delithiation process [6, 17, 18]. These merits attract a large amount of interest in exploring the synthetic processes of porous silicon anodes for LIBs [19-22]. Among them, reducing SiO$_2$ by magnesiothermic reduction is considered a promising approach to synthesizing porous silicon because of its controllable porosity and much lower reaction temperatures than conventional silicon productions [23-25]. Microsized-porous Si structures synthesized by MR reaction have been reported to have considerable cycling

performance [16, 26]. However, one defect of the microsized porous Si is its fragile mechanical strength due to weak and limited internal connections, which tend to fracture during cycling [26]. To support the porous Si structure and limit the side reaction between Si and electrolytes, graphene coating has been proposed and widely taken as an ideal approach due to its excellent resilience and high conductivity [27, 28]. Unfortunately, in most reports, graphene coatings are sophisticated and need harsh conditions during synthetic processes, making them very expensive and hard to scale up [29-31]. Because of this, low-cost graphene synthesized via economic approaches from abundant feedstock, like coal, is highly desirable and considered to be a promising approach [32-35]. Coal, a sedimentary rock composed predominantly of carbon, has proven to be an ideal material for a variety of applications [36, 37]. It is formed through the coalification of buried plant matter, during which the plant matter changes from cellulose, consisting of glucose (Figure 1), through peat, lignite, and bituminous coal to anthracite. In this evolution, high temperature and pressure facilitate the removal of functional groups (mostly H and O) and fuse carbon into benzene rings. When the coalification process comes to the anthracite, the benzene rings fuse together tightly, just as in graphite, making it insoluble and difficult to break into graphene.
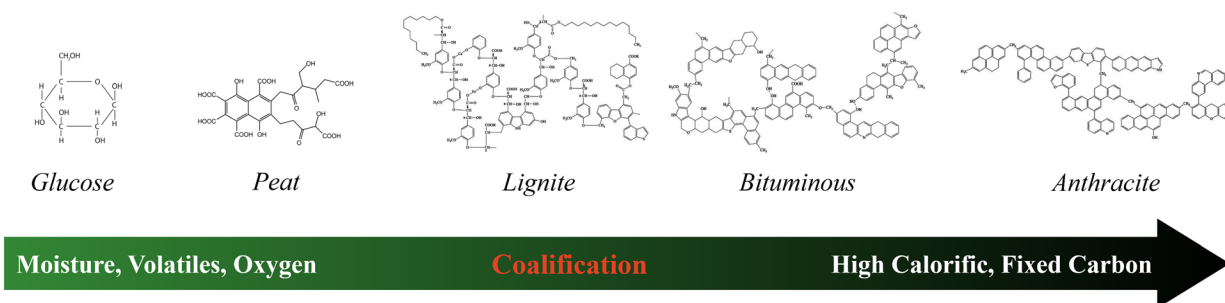

Figure 1. (2-column fitting image). Schematic of formula changes in the coalification process.

Thus, the intermediates in the coalification process, like low-rank coal with loose intermolecular bonding, show great potential in graphene coating for anode materials. Humic acid (HA) is the main organic matter of low-rank coal (lignite) with a molecular weight ranging from several hundred to millions [38]. Typically, HA is a kind of dark brown powder with two-thirds of the carbon atoms sp^2 hybridized, while the rest mainly exist in carboxyl groups or with hydroxyl groups (as shown in Figure S1). Unlike other graphene precursors such as graphite and coal tar pitch requiring complex processing, the abundant functional groups make HA soluble in water-based alkaline solutions and much easier to process for the production of graphene. The unique

structure enables HA to be a promising precursor for high-quality and large-scale graphene synthesis at a considerably low cost [33, 39, 40]. In this work, we use low-cost SiO_2 microspheres (SiO_2) in addition to HA. These materials supply the process to create micrometer-sized porous Si coated with a graphene coating (mpSi@G) (Figure 2a). The featured graphene coating and nano-porous Si (pSi) could be an efficient solution to release the mechanical stress of the Si anode upon lithiation. The high conductive graphene coating with plenty of defects also facilitates fast charging performance. Detailed electrochemical testing and characterizations were carried out to illuminate the effectiveness of the design.

2.   Experimental section

2.1.   Synthesis of the mpSi@G composite

0.8 g silica spheres (1000 nm, Alibaba) and 0.8 g Mg powder were combined and then dispersed in 6.0 g NaCl powder in an Ar-filled glovebox. The mix was then transferred to a metallic tube before being tightly sealed (Figure S2). The magnesiothermic reduction took place when the tube was heated to 700 ℃ and remained there for 5 h. The resulting powder was soaked in a 5% HCl solution and stirred overnight followed by D.I. water washing. The resulting porous Si nanoparticles were subsequently mixed with NH_3 solution (28 %, 1.0 mL), D.I. water (200 mL), and HA (0.3 g). Here, NH_3 provides a base environment in water to dissolve HA. After being vigorously stirred for 2 h, the above slurry was pumped into a spray dryer and spray-dried to form micrometer-sized Si/HA composite spheres. The powder from spray drying was carbonized for 2 h at 300 ℃ before being put under an Ar blanket at 800 ℃ for 5 h. After the calcination, the residual SiO_2 in the powder was removed with 5% HF solution for 5 min. Finally, a micrometer-sized porous Si@G composite (mpSi@G) was obtained. Commercial Si powder (micrometer-sized, MTI, USA) was named "bare Si" and used as a reference in this article.

2.2.   Materials characterization

Scanning electron microscopy (FEI Quanta 650 FEG SEM) incorporating an energy-dispersed X-ray (EDX) spectrometer was employed to analyze particle morphology and elemental composition. The mpSi@G particles were fixed in epoxy resin and then were polished to create cross-sections for observation. Powder X-ray diffraction (XRD) analysis was performed with a Smartlab X-ray diffractometer (Rigaku) operating at 40 kV and 44 mA. The radiation used was Cu Kα, with a scan rate of 3 °/min over the range of 10° to 80°. Automatic particle counting was conducted by ImageJ from SEM images to get the particle size distribution. Raman spectra were obtained from a Raman

Spectrometer (HORIBA) with a 532 nm laser and 1800 grating. A carbon analyzer (TOC-V, SHIMADZU) with an SSM5000A module was used to evaluate the content of carbon in the composite.

X-ray absorption near-edge structure (XANES) experiments were conducted at the VLS-PGM beamline situated within the Canadian Light Source, Saskatoon. The electrodes for testing were initially assembled in coin cells, lithiated to 0.01V, and disassembled to remove the electrodes. Acetonitrile (>99.5%, Fisher Chemical) was then used to rinse them. Post-cleaning and drying, the electrodes were affixed to sample holders and then placed in the testing chamber of the VLS-PGM endstation. XANES spectra were simultaneously obtained in two modes: total electron yield (TEY) and (FLY). TEY data for the sample were collected via measurement of the drain current, while FLY data were collected via a multichannel plate detector. Throughout these tests, the test chamber was kept in a high vacuum condition (lower than 1×10^{-7} Torr). Data normalization was achieved using the I_0 current, obtained through a nickel mesh positioned ahead of the sample. The beamline energy calibration was conducted with reference to the LiCl signal observed at 61-62 eV. For detailed operational procedures, please refer to ref. [41].

2.3.   Electrochemical measurements

The electrode paste formulation involved mixing mpSi@G composite, a conductive agent (Carbon nanotube), and CMC (Carboxymethyl Cellulose) at a mass ratio of 90: 4: 6 in D.I. water. After thoroughly mixing the paste, it was spread on copper foil, laminated, and allowed to dry in the vacuum oven overnight at 80 ℃. The resulting coating was then punched into disk-shaped electrodes. The active materials loading on the electrodes is ~ 0.90 mg cm^{-2}. Afterward, the electrode disks were used as the working electrodes to assemble CR2032 coin cells under a pure Ar atmosphere. In the coin cells, lithium foil was used as the counter electrodes, Celgard 2400 film as the separator, and 1.2 M LiPF$_6$ in EC/DMC/EMC (1/1/1) with 10 wt% FEC as the electrolyte. A Neware Battery testing apparatus (Neware, China) was used to evaluate the cycling and rate performance of the assembled cells. The charge-discharge tests ranged between 0.01 V and 2.0 V (vs. Li/Li$^+$). Electrochemical impedance spectroscopy (EIS) analyses were conducted using a Gamry Interface 1010E potentiostat (Gamry Instrument, USA) with an AC voltage amplitude of 5 mV across a frequency range from 1 MHz down to 0.01 Hz. Cyclic voltammetry (CV) analyses were also performed using the potentiostat with a scanning voltage range of 0.01-1.5 V at a scan rate of 0.1 mV S^{-1}.
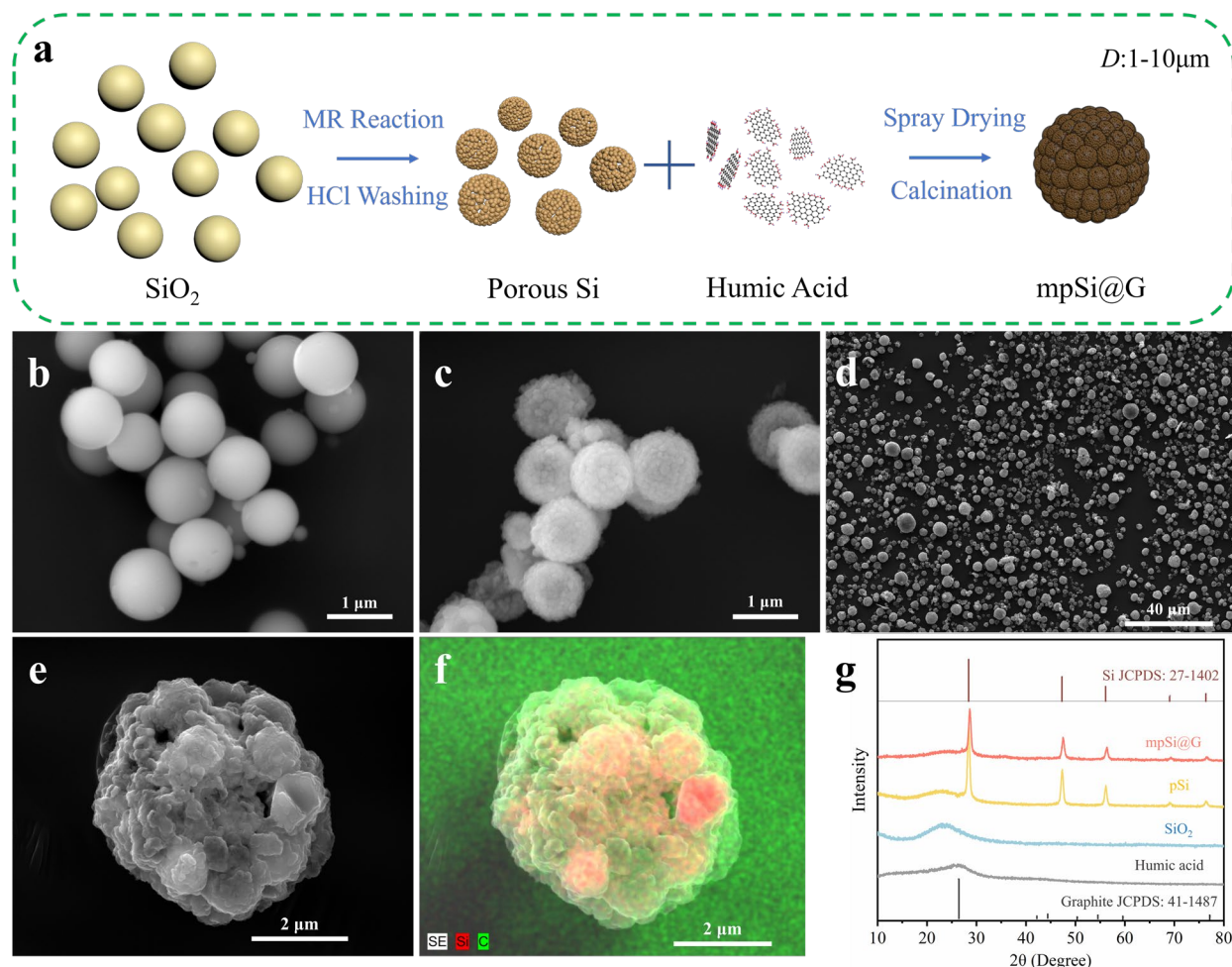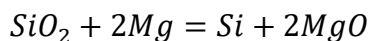
3. Results and discussion

Figure 2. (2-column fitting image). (a) Depiction of the fabrication process of the mpSi@C composite. SEM images of (b) SiO$_2$ particles, (c) porous Si particles, (d) the mpSi@G composite, (e) a magnified SEM image of a mpSi@G sphere, and (f) its elemental mapping. (g) XRD patterns of SiO$_2$, pSi, and mpSi@G.

In this work (Figure 2a), the mpSi@G composite was synthesized through MR reaction, spray drying, and calcination. The morphology of the intermediates during the synthetic process was examined by SEM, with Figure 2b showing that the SiO$_2$ used in this work consists of spherical particles with a size averaging 1000 nm. In the following MR reaction, the SiO$_2$ particles reacted with the Mg vapor formed by the sublimation of Mg powder at high temperatures, forming Si and MgO composite [23, 24]:

$$SiO_2 + 2Mg = Si + 2MgO$$

The unwanted MgO was removed by a following HCl washing, leaving the spherical porous Si particles (Figure 2c) with a size distribution identical to SiO_2. The obtained pSi was further mixed with HA slurry for spray drying. The spray-drying process introduced in this work has proven to be a successful method for particle assembly [42, 43]. During spray-drying, porous Si and HA slurry were atomized into mist, which consists of many tiny slurry droplets. The solvent in the droplets evaporated instantly by hot dry air, leaving secondary microsized spherical pSi@HA particles to be collected. The final calcination removed H and O atoms from HA and left graphene coatings on the porous Si, forming the mpSi@G composite. The carbon content of the mpSi@G is measured to be 21.1% by the carbon analyzer. As shown in Figure 2d, the dominant mpSi@G particles are spherical, with the particle size ranging from 1-10 μm (Figure S3). The magnified SEM image of a mpSi@G particle (Figure 2e) illuminates the spherical secondary structure. The corresponding EDS elemental mapping (Figure 2f) further reveals the positioning of silicon and carbon in the secondary structure, where porous Si particles constitute the main body of the particle and are still intact even after spray drying and calcination. As indicated by carbon mapping, these porous Si particles are connected and coated by a hierarchical carbon network. The connecting carbon inside the mpSi@G makes the composite more conductive [28], while the outer layer of carbon blocks side reactions between Si and the electrolytes, resulting in higher electrochemical performance during cycling [40]. The XRD patterns in Figure 2g confirm the proposed phase change in the synthetic process. The broad peak of SiO_2 powder located in $2\theta = 15 - 25°$ indicates its amorphous nature. After the MR reaction and HCl washing, high-purity porous Si was collected as all of its peaks belong to the standard Si phase (JCPDS 27-1402). The final mpSi@G composite obtained retains its purity even after spray-drying and calcination.
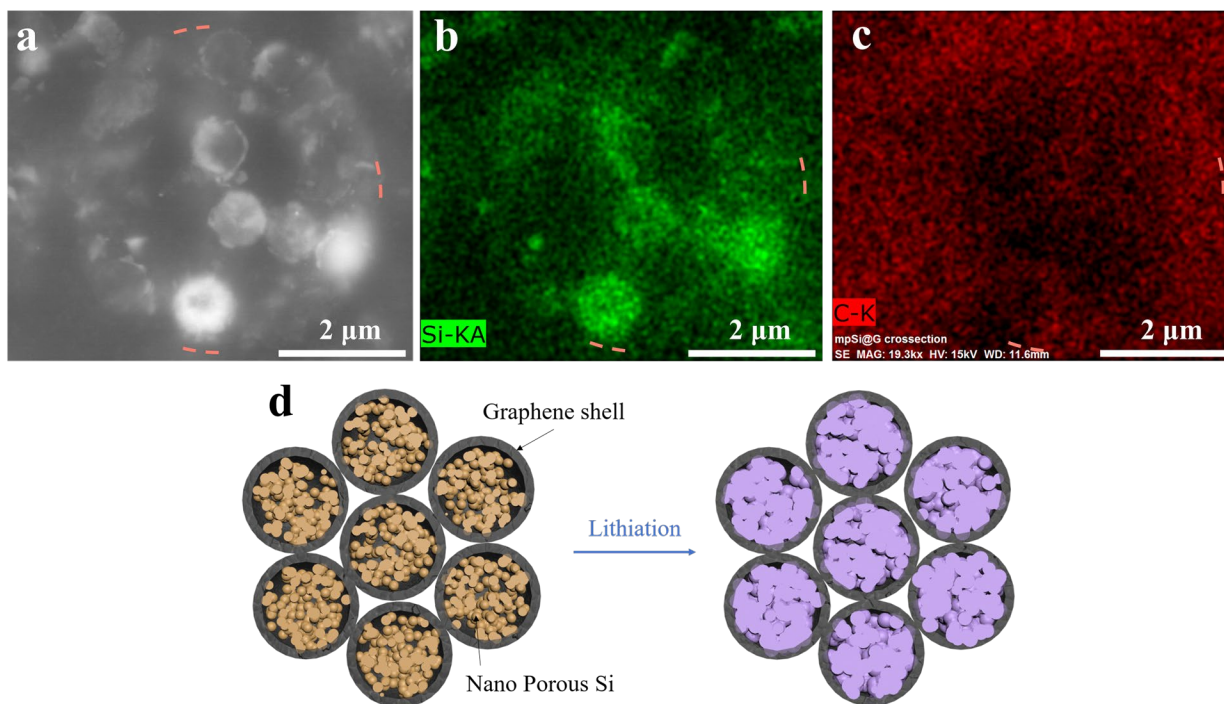
Figure 3. (2-column fitting image). (a) Cross-sectional SEM (BSE) image and the related EDS Si (b) and carbon (c) mapping of a mpSi@G particle. (d) Illustration of the hierarchical and porous structure in lithiation accommodating Si expansion.

The cross-section of a mpSi@G particle shown in Figure 3a reveals its internal structure and composition, where primary particles remain spherical and porous interconnecting with each other. The corresponding EDS Si mapping displays (Figure 3b) the presence of Si, demonstrating the primary particles are made of Si. The associated EDS carbon mapping (Figure 3c) shows the presence of carbon in the cross-section. It can be observed that the bright Si particles shown in the EDS Si mapping (Figure 3b) turn into darker spots in the carbon mapping (Figure 3c), indicating carbon exists mostly outside of the nanoporous Si as graphene shells. In this hierarchical arrangement, the graphene shelling encapsulating porous Si (Figure 3d) could effectively release the mechanical stress of the Si anode created during lithiation without breaking the graphene shell and the as-formed SEI film. It is worth noting that, unlike most reports that have achieved this pomegranate-like structure by sophisticated processes and harsh conditions, [22, 44, 45], this spray drying approach is straightforward and promising to scale up without complicated synthetic conditions.
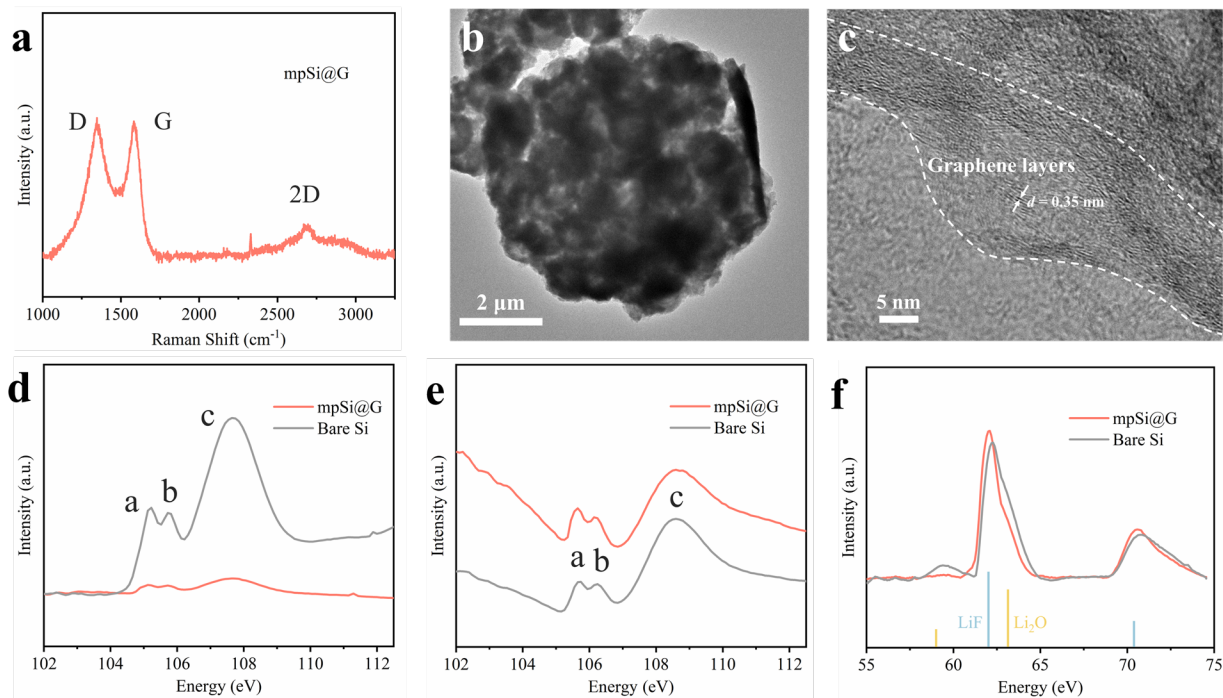
8

Figure 4. (2-column fitting image). (a) Raman spectra of the mpSi@G. (b) TEM image of a mpSi@G particle and (c) the graphene layers coated on the mpSi@G surface. (d) Si L-edge XANES (TEY) spectra and (e) Si L-edge XANES (FLY) spectra of the mpSi@G and bare Si. (f) Li K-edge XANES (FLY) spectra of fully lithiated mpSi@G and bare Si.

The nature of the carbon material in mpSi@G was explored deeper through Raman spectroscopy. The distinct G-band at 1585 cm^{-1} and the 2D peak at 2663 cm^{-1}, as shown in Figure 4a, demonstrate the carbon shell is graphene. A noticeable D-band at 1351 cm^{-1} highlights the presence of numerous defects, which are crucial for enhancing the movement of Li-ions through the graphene layer. The TEM image of a mpSi@G particle (Figure 4b) confirms the hierarchical structure, where the porous Si bead clusters are enclosed by a graphene coating. HRTEM of the graphene coating (Figure 4c) shows the clear graphene layers with an interlayer spacing of 0.35 nm. Plenty of defects in the graphene coating allow Li ions to penetrate and extract freely, facilitating high-rate capability. Si and Li's XANES spectra as effective tools to examine the surface features and chemical makeup of mpSi@G were collected and analyzed. Figure 4d shows the Si L-edge XANES spectra in TEY mode, which has a detecting depth of a few nanometers. Peak a, b, and c belong to the excitation of Si 2p orbitals [46, 47], which are significant in the bare Si, but delicate in mpSi@G, indicating an intact graphene coating on porous Si. The Si L-edge XANES spectra in

FLY mode (Figure 4e) give in-depth detection (~ 60 nm, Figure S4a) and are thus capable of exploring the Si-O-C interface in mpSi@G. The relative peak ratio of peaks a and b can be attributed to the long-range order of Si-O tetrahedral coordination. Compared to bare Si, the high peak ratio in mpSi@G indicates strong Si-O-C bonding, which makes the structure of mpSi@G more durable in battery cycling [48].

Li K-edge XANES (FLY) spectra for both fully lithiated mpSi@G and pure Si are displayed in Figure 4f. The graph's peaks correspond to two distinct substances, LiF (noted at 62 and 71 eV) and Li_2O (identified at 58 and 63 eV), as referenced in the lithium compounds XANES database [41]. The presence of Li_2O is attributed to the breakdown of two volatile SEI components, Li_2O_2 and Li_2CO_3, triggered by soft X-ray exposure during XANES analysis [49]. In the Li K-edge excitation range of 50–75 eV, the penetration depth reaches approximately 15 nm (see Figure S4b), providing an optimal depth for studying the SEI formation and its chemical composition during the first stages of lithiation. The enhanced intensity of Li_2O peaks in pure Si suggests a higher degree of adverse reactions between Si and electrolytes, forming a thick SEI. The carbon coating in mpSi@G effectively confines SEI growth, leading to a more stable electrode interface [50].
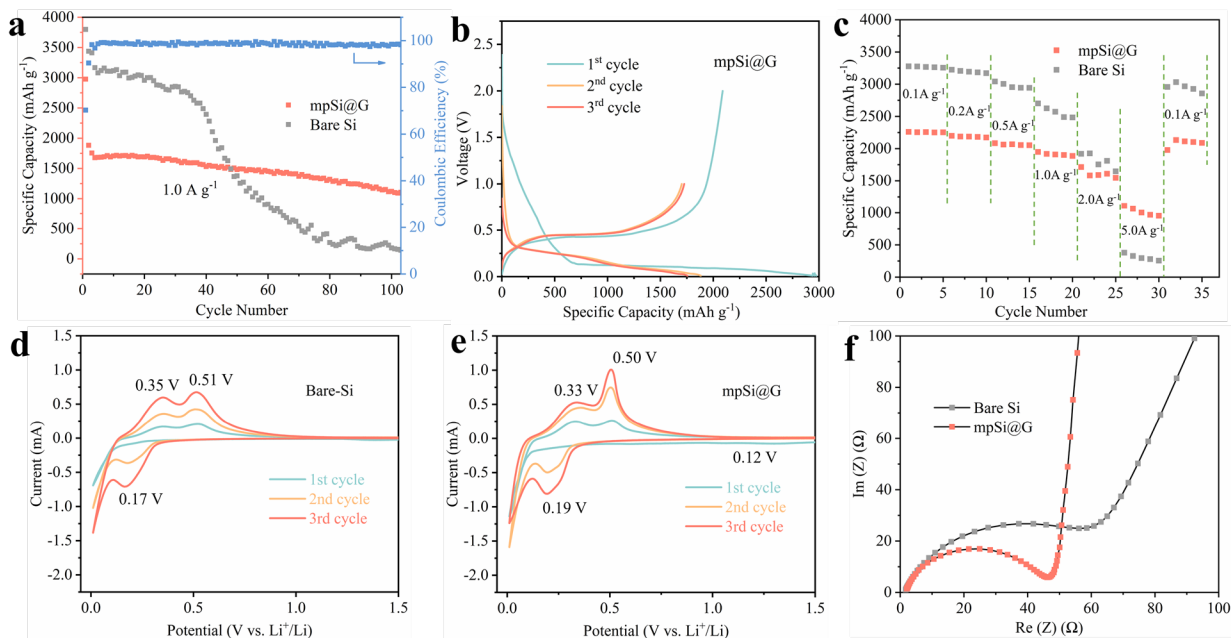

Figure 5. (2-column fitting image). (a) Cycling properties and coulombic efficiency of mpSi@G along with the cycling results of bare Si at 1.0 A g^{-1}. (b) The initial three cycles of charge-discharge profiles for mpSi@G. (c) Performance at various rates for electrodes made of bare-Si and mpSi@G.

(d) Cyclic voltammetry curves of bare-Si and (e) mpSi@G at a scanning speed of 0.1 mV S^{-1} over the first 3 cycles. (f) Pre-cycling Nyquist plots of electrodes of both bare-Si and mpSi@G.

Cycling and rate testing results further reveal a remarkable electrochemical improvement over bare Si. The mpSi@G presents a considerable initial discharge capacity of 2974.9 mAh g^{-1} at 0.1 A g^{-1} (Figure 5a). The capacity is inferior to that of bare Si, which stands at 3796.8 mAh g^{-1}. Nonetheless, the strategic hierarchical architecture of mpSi@G ensures a considerable cycling performance at 1.0 A g^{-1}, maintaining 66% of its capacity after 100 cycles. During cycling, the mpSi@G (Figure 5b) presents typical charge-discharge profiles of Si anodes with clear lithiation and delithiation plateaus. The capacity of bare Si first drops gradually, then considerably decreases after 30 cycles. The mpSi@G and bare Si electrodes were charged/discharged at a series of current densities to evaluate their rate capabilities. The mpSi@G composite (Figure 5c) delivers reversible capacities of 2259.9, 2198.4, 2084.2, 1948.1, 1713.8, and 1109.5 mAh g^{-1} at the charge/discharge current densities of 0.1, 0.2, 0.5, 1.0, 2.0, and 5.0 A g^{-1}, respectively. Remarkably, the capacity nearly returns to its initial level when the current density reverts to 0.1 A g^{-1}. The mpSi@G composite in the work displays both high charge/discharge capacity and considerable capacity retention compared to the Si/C composites with similar structures from other teams (Table S1). Conversely, the capacity of bare Si significantly diminishes as current density increases, primarily due to its poor conductivity, presenting a capacity of 379.5 mAh g^{-1} at 5.0 A g^{-1}. The mpSi@G electrode after cycling was rinsed by 1,2-Dimethoxyethane (DME) to remove residual electrolyte and then was dried for SEM characterization as shown in Figure S5. After cycling, the electrode coating (Figure S5c) still even sticks to the Cu current collector without any exfoliation or crack compared to the pristine electrode surface (Figure S5a). In the HR SEM image after cycling, Most of the spheres (Figure S5d) remain intact despite some SEI can be found on the surface of the coating, indicating a superior cycling stability. The mpSi@G composite's superior cycling and rate capability is attributed to three key factors: 1) the nanoporous Si structure allows the Si to expand and contract during the charge and discharge processes while still keeping the surrounding carbon shell intact, 2) the highly graphitized carbon structure brings high electrical conductivity for charge transfer through the whole micrometer-sized particle, resulting in a high rate performance, and 3) the external carbon coating effectively shield the encapsulated Si from electrolyte interactions, minimizing growth of the SEI.

The CV curves in Figures 5d and 5e describe the first three scanning cycles of the bare-Si and mpSi@G. The initial mpSi@G cathodic scan reveals a broad peak at 1.2 V caused by the SEI formation at the interface of the carbon shell and the electrolyte [51, 52]. The reduction peak in the range of 0.01-0.2 V is associated with the lithiation of the Si phase in bare Si and mpSi@G. The two oxidation peaks in the de-lithiation process, situated at 0.35 and 0.51 V for bare Si and slightly adjusted to 0.33 and 0.50 V for mpSi@G, can be attributed to the removal of lithium ions from the as-formed Li_xSi alloy [52, 53]. The peak current increases gradually from the first to the third cycle as more Si participates in the alloying process. The difference in redox peak potentials (ΔE_p) shows a narrower span for mpSi@G (0.01 to 0.49 V) compared to bare Si (0.01 to 0.51 V), implying more rapid electrochemical kinetics in mpSi@G attributable to its hierarchical structure that promotes faster electron and Li-ion movement. Additionally, these discussions are supported by the Nyquist results (Figure 5f) gathered from EIS testing. One depressed semicircle is seen in the Nyquist plots for both bare Si and mpSi@G in the high-frequency range, relating to charge-transfer resistance. While in the low-frequency range, however, an inclined line is seen which is associated with Li^+ diffusion [54]. The significantly reduced charge-transfer resistance of the mpSi@G composite, as evidenced by its smaller semicircle, indicates its enhanced electrochemical performance compared to bare Si.

4.   Conclusions

To conclude, we have successfully demonstrated a viable method for creating a mpSi@G composite using SiO_2 particles and coal-derived HA. The strategically designed hierarchical carbon architecture is conducive to high conductivity, while also preventing unwanted reactions between the electrolyte and the porous Si embedded within, thereby significantly enhancing the composite's electrical conductivity. Consequently, the mpSi@G showcases a remarkable cycling performance, as it maintains 66% of its capacity after 100 cycles, along with outstanding rate capability, delivering 1109.5 mAh g^{-1} at the current density of 5.0 A g^{-1}. This work provides a novel and effective approach to improving the Si anode performance for the LIB industry.

CRediT authorship contribution statement

Shuai Xu: Conceptualization, Methodology, Validation, Formal analysis, Investigation, Writing - Original Draft, Visualization. **Jigang Zhou:** Formal analysis, review & editing. **Lucia Zuin:**

Investigation, Formal analysis, review & editing. **Di Sun:** Resources, Investigation. **Julia Zhao:** Project administration, funding acquisition, supervision. **Abdelmalek Bellal:** Formal analysis, review & editing. **Xiaodong Hou:** Methodology, Writing - Review & Editing, Project administration, Funding acquisition, Supervision.

Supplementary materials

Supplementary materials associated with this article can be found in the online version.

Declaration of Competing Interest

The authors declare no competing financial interest.

Acknowledgements

References

[1] M. Armand, J.-M. Tarascon, Building Better Batteries, Nature, 451 (2008) 652.

[2] C.-M. Park, J.-H. Kim, H. Kim, H.-J. Sohn, Li-alloy Based Anode Materials for Li Secondary Batteries, Chem. Soc. Rev., 39 (2010) 3115-3141.

[3] D. Ma, Z. Cao, A. Hu, Si-based Anode Materials for Li-Ion Batteries: A Mini Review, Nano-Micro Lett., 6 (2014) 347-358.

[4] W.U. Rehman, H. Wang, R.Z.A. Manj, W. Luo, J. Yang, When Silicon Materials Meet Natural Sources: Opportunities and Challenges for Low‐Cost Lithium Storage, Small, (2019) 1904508.

[5] F. Shi, Z. Song, P.N. Ross, G.A. Somorjai, R.O. Ritchie, K. Komvopoulos, Failure Mechanisms of Single-Crystal Silicon Electrodes in Lithium-ion Batteries, Nat. Commun., 7 (2016) 11886.

[6] M. Ge, X. Fang, J. Rong, C. Zhou, Review of Porous Silicon Preparation and its Application for Lithium-Ion Battery Anodes, Nanotechnology, 24 (2013) 422001.

[7] X.H. Liu, L. Zhong, S. Huang, S.X. Mao, T. Zhu, J.Y. Huang, Size-Dependent Fracture of Silicon Nanoparticles During Lithiation, ACS nano, 6 (2012) 1522-1531.

[8] M. Gu, Y. He, J. Zheng, C. Wang, Nanoscale Silicon as Anode for Li-Ion Batteries: The Fundamentals, Promises, and Challenges, Nano Energy, 17 (2015) 366-383.

[9] B. Wang, X. Li, T. Qiu, B. Luo, J. Ning, J. Li, X. Zhang, M. Liang, L. Zhi, High Volumetric Capacity Silicon-Based Lithium Battery Anodes by Nanoscale System Engineering, Nano Lett., 13 (2013) 5578-5584.

[10] J.R. Szczech, S. Jin, Nanostructured Silicon for High Capacity Lithium Battery Anodes, Energy Environ. Sci., 4 (2011) 56-72.

[11] U. Kasavajjula, C. Wang, A.J. Appleby, Nano-and Bulk-Silicon-Based Insertion Anodes for Lithium-Ion Secondary Cells, J. Power Sources, 163 (2007) 1003-1039.

[12] C.K. Chan, H. Peng, G. Liu, K. McIlwrath, X.F. Zhang, R.A. Huggins, Y. Cui, High-Performance Lithium Battery Anodes Using Silicon Nanowires, Nat. Nanotechnol., 3 (2008) 31-35.

[13] J. Hu, Y. Bando, Z. Liu, J. Zhan, D. Golberg, T. Sekiguchi, Synthesis of Crystalline Silicon Tubular Nanostructures with ZnS Nanowires as Removable Templates, Angew. Chem., 116 (2004) 65-68.

[14] M.-H. Park, M.G. Kim, J. Joo, K. Kim, J. Kim, S. Ahn, Y. Cui, J. Cho, Silicon Nanotube Battery Anodes, Nano Lett., 9 (2009) 3844-3847.

[15] N. Liu, H. Wu, M.T. McDowell, Y. Yao, C. Wang, Y. Cui, A Yolk-Shell Design for Stabilized and Scalable Li-Ion Battery Alloy Anodes, Nano Lett., 12 (2012) 3315-3321.

[16] H. Jia, J. Zheng, J. Song, L. Luo, R. Yi, L. Estevez, W. Zhao, R. Patel, X. Li, J.-G. Zhang, A Novel Approach to Synthesize Micrometer-Sized Porous Silicon as A High Performance Anode for Lithium-Ion Batteries, Nano Energy, 50 (2018) 589-597.

[17] M. Ge, Y. Lu, P. Ercius, J. Rong, X. Fang, M. Mecklenburg, C. Zhou, Large-Scale Fabrication, 3D Tomography, and Lithium-Ion Battery Application of Porous Silicon, Nano Lett., 14 (2014) 261-268.

[18] Q. Xiao, M. Gu, H. Yang, B. Li, C. Zhang, Y. Liu, F. Liu, F. Dai, L. Yang, Z. Liu, Inward Lithium-Ion Breathing of Hierarchically Porous Silicon Anodes, Nat. Commun., 6 (2015) 1-8.

[19] M. Ge, J. Rong, X. Fang, A. Zhang, Y. Lu, C. Zhou, Scalable Preparation of porous Silicon Nanoparticles and Their Application for Lithium-Ion Battery Anodes, Nano Res., 6 (2013) 174-181.

[20] Y. Lai, J.R. Thompson, M. Dasog, Metallothermic Reduction of Silica Nanoparticles to Porous Silicon for Drug Delivery Using New and Existing Reductants, Chem. Eur. J., 24 (2018) 7913-7920.

[21] G. Shivaraju, C. Sudakar, A. Prakash, High-Rate and Long-Cycle Life Performance of Nano-Porous Nano-Silicon Derived from Mesoporous MCM-41 as An Anode for Lithium-Ion Battery, Electrochim. Acta, 294 (2019) 357-364.

[22] N. Liu, Z. Lu, J. Zhao, M.T. McDowell, H.-W. Lee, W. Zhao, Y. Cui, A Pomegranate-Inspired Nanoscale Design for Large-Volume-Change Lithium Battery Anodes, Nat. Nanotechnol., 9 (2014) 187-192.

[23] J. Entwistle, A. Rennie, S. Patwardhan, A Review of Magnesiothermic Reduction of Silica to Porous Silicon for Lithium-Ion Battery Applications and Beyond, J. Mater. Chem. A, 6 (2018) 18344-18356.

[24] L. Shi, W. Wang, A. Wang, K. Yuan, Y. Yang, Understanding the impact mechanism of the thermal effect on the porous silicon anode material preparation via magnesiothermic reduction, J. Alloys Compd., 661 (2016) 27-37.

[25] Z. Bao, M.R. Weatherspoon, S. Shian, Y. Cai, P.D. Graham, S.M. Allan, G. Ahmad, M.B. Dickerson, B.C. Church, Z.J.N. Kang, Chemical Reduction of Three-Dimensional Silica Micro-Assemblies into Microporous Silicon Replicas, 446 (2007) 172-175.

[26] W. Wang, Z. Favors, R. Ionescu, R. Ye, H.H. Bay, M. Ozkan, C.S. Ozkan, Monodisperse Porous Silicon Spheres as Anode Materials for Lithium Ion Batteries, Sci. Rep., 5 (2015) 8781.

[27] G. Kucinskis, G. Bajars, J. Kleperis, Graphene in Lithium Ion Battery Cathode Materials: A Review, J. Power Sources, 240 (2013) 66-79.

[28] H. Li, H. Zhou, Enhancing the Performances of Li-ion Batteries by Carbon-Coating: Present and Future, Chem. Commun., 48 (2012) 1201-1217.

[29] I.H. Son, J.H. Park, S. Kwon, S. Park, M.H. Rümmeli, A. Bachmatiuk, H.J. Song, J. Ku, J.W. Choi, J.-m. Choi, Silicon Carbide-free Graphene Growth on Silicon for Lithium-ion Battery with High Volumetric Energy Density, Nat. Commun., 6 (2015) 7393.

[30] Y. Li, K. Yan, H.-W. Lee, Z. Lu, N. Liu, Y. Cui, Growth of Conformal Graphene Cages on Micrometre-Sized Silicon Particles as Stable Battery Anodes, Nat. Energy, 1 (2016) 15029.

[31] M.F. El-Kady, Y. Shao, R.B. Kaner, Graphene for Batteries, Supercapacitors and Beyond, Nat. Rev. Mater., 1 (2016) 1-14.

[32] J. Wu, Y. Cao, H. Zhao, J. Mao, Z. Guo, The Critical Role of Carbon in Marrying Silicon and Graphite Anodes for High‐Energy Lithium‐Ion Batteries, Carbon Energy, (2019).

[33] C. Powell, G.W. Beall, Graphene Oxide and Graphene from Low Grade Coal: Synthesis, Characterization and Applications, Curr. Opin. Colloid Interface Sci., 20 (2015) 362-366.

[34] S.H. Choi, G. Nam, S. Chae, D. Kim, N. Kim, W.S. Kim, J. Ma, J. Sung, S.M. Han, M. Ko, Robust Pitch on Silicon Nanolayer–Embedded Graphite for Suppressing Undesirable Volume Expansion, Adv. Energy Mater., 9 (2019) 1803121.

[35] G.W. Beall, E.-S.M. Duraia, Q. Yu, Z. Liu, Single Crystalline Graphene Synthesized by Thermal Annealing of Humic Acid over Copper Foils, Physica E Low Dimens. Syst. Nanostruct., 56 (2014) 331-336.

[36] S.P. Sasikala, L. Henry, G. Yesilbag Tonga, K. Huang, R. Das, B. Giroire, S. Marre, V.M. Rotello, A. Penicaud, P. Poulin, High Yield Synthesis of Aspect Ratio Controlled Graphenic Materials from Anthracite Coal in Supercritical Fluids, ACS nano, 10 (2016) 5293-5303.

[37] R. Ye, C. Xiang, J. Lin, Z. Peng, K. Huang, Z. Yan, N.P. Cook, E.L. Samuel, C.-C. Hwang, G. Ruan, Coal as an Abundant Source of Graphene Quantum Dots, Nat. Commun., 4 (2013) 1-7.

[38] F.J. Stevenson, Humus chemistry: genesis, composition, reactions, John Wiley & Sons1994.

[39] M.D. El-shazly, B. Henderson, G.W. Beall, Reduced Humic Acid Nanosheets and its Uses as Nanofiller, J. Phys. Chem. Solids, 85 (2015) 86-90.

[40] S. Xu, J. Zhou, J. Wang, S. Pathiranage, N. Oncel, P. Robert Ilango, X. Zhang, M. Mann, X. Hou, In Situ Synthesis of Graphene‐Coated Silicon Monoxide Anodes from Coal‐Derived Humic Acid for High‐Performance Lithium‐Ion Batteries, Adv. Funct. Mater., 31 (2021) 2101645.

[41] D. Wang, L. Zuin, Li K-edge X-ray Absorption Near Edge Structure Spectra for A Library of Lithium compounds Applied in Lithium Batteries, J. Power Sources, 337 (2017) 100-109.

[42] S. Xu, X.-Y. Lv, Z. Wu, Y.-F. Long, J. Su, Y.-X. Wen, Synthesis of Porous-Hollow $LiMn0.85Fe0.15PO4/C$ Microspheres as A Cathode Material for Lithium-Ion Batteries, Powder Technol., 308 (2017) 94-100.

[43] H. Tao, L. Xiong, S. Zhu, L. Zhang, X. Yang, Porous Si/C/Reduced Graphene Oxide Microspheres by Spray Drying as Anode for Li-Ion Batteries, J. Electroanal. Chem., 797 (2017) 16-22.

[44] N. Ding, Y. Chen, R. Li, J. Chen, C. Wang, Z. Li, S. Zhong, Pomegranate Structured C@ pSi/rGO Composite as High Performance Anode Materials of Lithium-Ion Batteries, Electrochim. Acta, 367 (2021) 137491.

[45] P. Wu, B. Shi, H. Tu, C. Guo, A. Liu, G. Yan, Z. Yu, Pomegranate-Type Si/C Anode with SiC Taped, Well-Dispersed Tiny Si Particles for Lithium-Ion Batteries, J. Adv. Ceram., 10 (2021) 1129-1139.

[46] M. Kasrai, W. Lennard, R. Brunner, G. Bancroft, J. Bardwell, K. Tan, Sampling Depth of Total Electron and Fluorescence Measurements in Si L-and K-Edge Absorption Spectroscopy, Appl. Surf. Sci., 99 (1996) 303-312.

[47] M. Kasrai, Z. Yin, G.M. Bancroft, K.H. Tan, X‐Ray Fluorescence Measurements of X‐Ray Absorption Near Edge Structure at The Si, P, and SL Edges, J. Vac. Sci. Technol, 11 (1993) 2694-2699.

[48] J. Zhou, Y. Hu, X. Li, C. Wang, L. Zuin, Chemical Bonding in Amorphous Si-Coated Carbon Nanotubes as Anodes for Li Ion Batteries: A XANES Study, RSC Adv., 4 (2014) 20226-20229.

[49] R. Qiao, Y.-D. Chuang, S. Yan, W. Yang, Soft X-ray Irradiation Effects of Li2O2, Li2CO3 and Li2O Revealed by Absorption Spectroscopy, PloS one, 7 (2012) e49182.

[50] S. Xu, X. Hou, D. Wang, L. Zuin, J. Zhou, Y. Hou, M. Mann, Insights into the Effect of Heat Treatment and Carbon Coating on the Electrochemical Behaviors of SiO Anodes for Li‐Ion Batteries, Adv. Energy Mater., 12 (2022) 2200127.

[51] Q. Xie, S. Qu, P. Zhao, A Facile Fabrication of Micro/Nano-Sized Silicon/Carbon Composite with A Honeycomb Structure as High-Stability Anodes for Lithium-Ion Batteries, J. Electroanal. Chem., 884 (2021) 115074.

[52] J. Chen, X. Guo, M. Gao, J. Wang, S. Sun, K. Xue, S. Zhang, Y. Liu, J. Zhang, Self-supporting dual-confined porous Si@ c-ZIF@ carbon nanofibers for high-performance lithium-ion batteries, Chemical Communications, 57 (2021) 10580-10583.

[53] H. Gu, M. Gao, K. Shen, T. Zhang, J. Zhang, X. Zheng, X. Guo, Y. Liu, F. Cao, H. Gu, F127 assisted fabrication of Ge/rGO/CNTs nanocomposites with three-dimensional network structure for efficient lithium storage, Chinese Chemical Letters, (2023) 109273.

[54] J. Cui, Y. Cui, S. Li, H. Sun, Z. Wen, J. Sun, Microsized Porous SiOx@C Composites Synthesized through Aluminothermic Reduction from Rice Husks and Used as Anode for Lithium-Ion Batteries, ACS Appl. Mater. Interfaces, 8 (2016) 30239-30247.

Supporting information for

Synthesis of Hierarchical Graphene Coated Porous Si Anode for High-performance Lithium-Ion Batteries

Shuai Xu,[a] Jigang Zhou,[b] Lucia Zuin,[b] Di Sun,[c] Julia Zhao,[c] Abdelmalek Bellal,[a] and Xiaodong Hou[*,a]

[a] College of Engineering and Mine, University of North Dakota, Grand Forks, North Dakota, 58202, United States

[b] Canadian Light Source Inc., Saskatoon, S7N 2V3, Canada

[c] Department of Chemistry, University of North Dakota, Grand Forks, North Dakota, 58202, United States

[*] Corresponding author. Email address: xiaodong.hou@und.edu
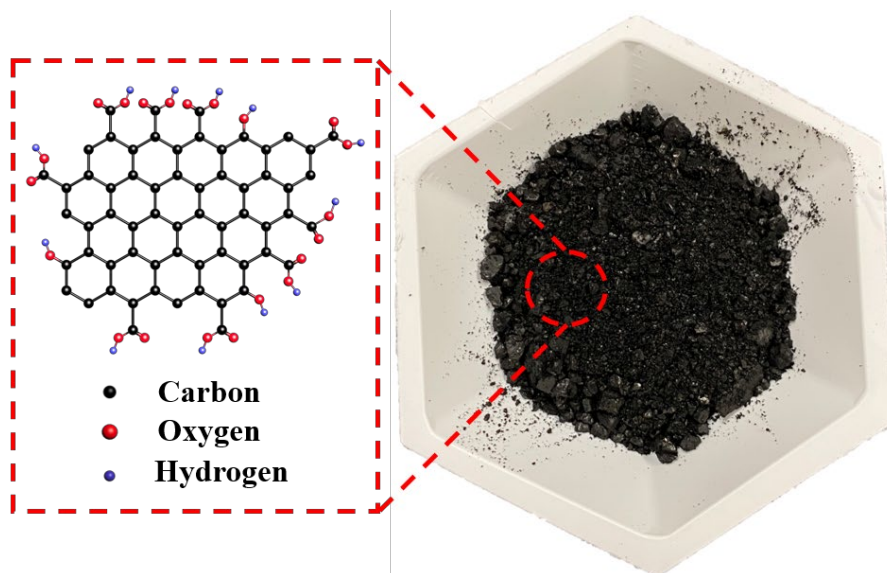
Figure S1. Humic acid and its typical molecular structure.

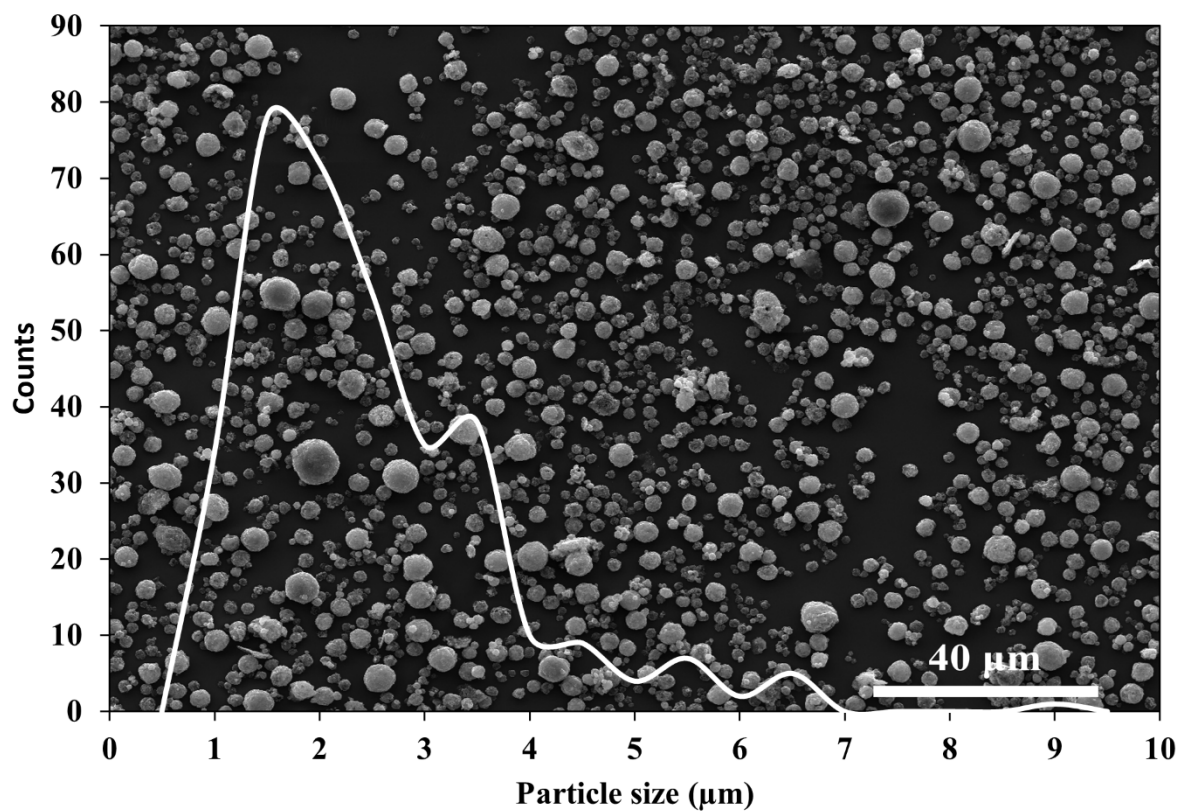
Figure S2. Stainless steel tube for MR reaction.

Figure S3. Particle size distribution of the mpSi@G powder corresponding the SEM image.
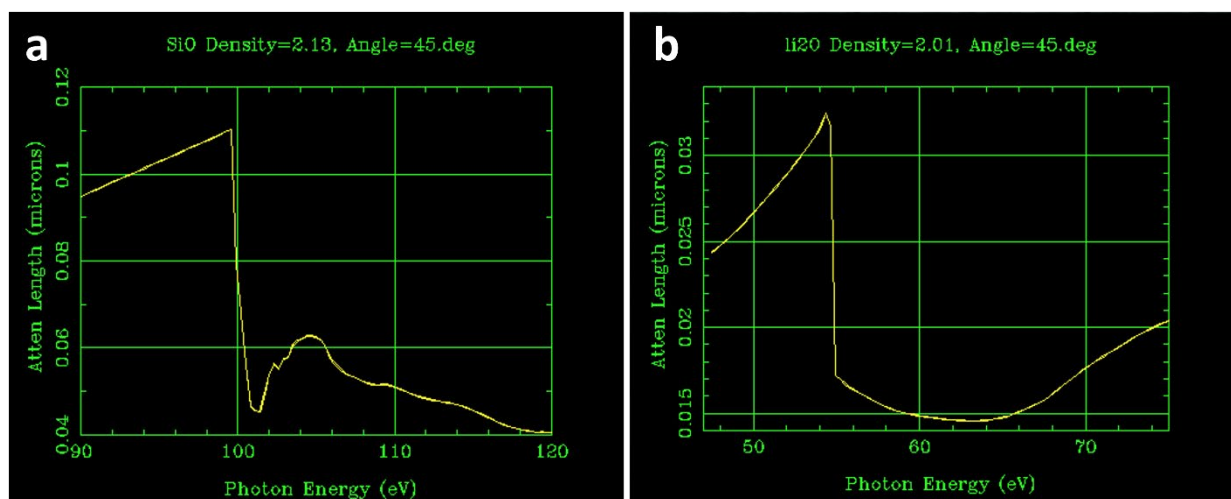

Figure S4. Detection depth of Si-L edge (a) and Li-K edge (b) XANES testing.

Table S1. The morphology and electrochemical performance of Porous Si and carbon composites [1].

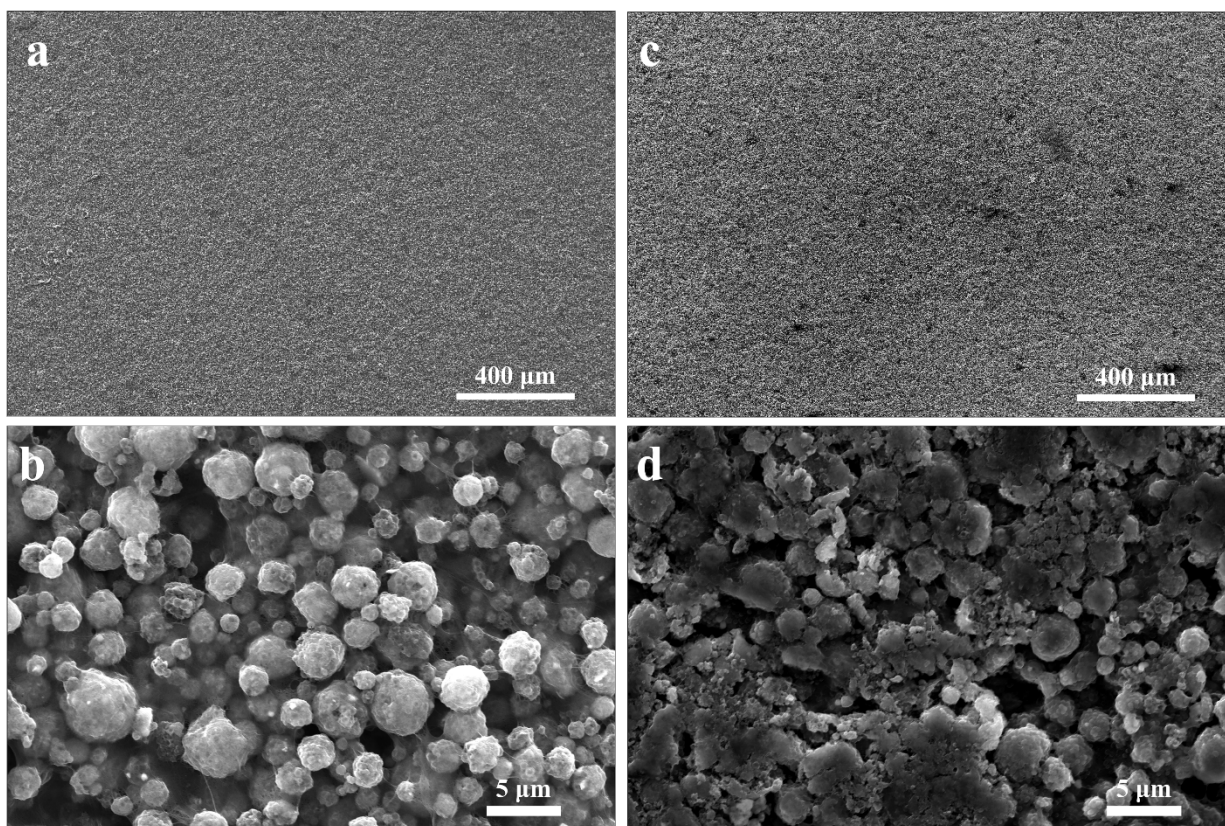| References	Morphology	Initial discharge capacity (mAh g^{-1})	ICE	Capacity retention
[2]	Porous Si/Cu/CNT/C	2734.1	72.6%	64% after 100 cycles
[3]	Porous Si/C	2047	84.6%	60% after 200 cycles
[4]	Nano Si wrapped with rGO	2628	~61%	~76.6% after 50 cycles
[5]	Porous SiOx wrapped in rGO	3765	68.1%	~15% after 200 cycles
[6]	Hollow Si/G composite	2383.2	66.1%	~50% after 100 cycles
This work	Micro-porous Si@G composite	2974.9	70.2%	66% after 100 cycles

Figure S5. SEM images of the mpSi@G electrodes before (a and b) and after (c and d) cycling at 5 A g^{-1} for 100 cycles.

References

[1] A.P. Yuda, P.Y.E. Koraag, F. Iskandar, H.S. Wasisto, A. Sumboja, Advances of the top-down synthesis approach for high-performance silicon anodes in Li-ion batteries, Journal of Materials Chemistry A, 9 (2021) 18906-18926.

[2] Z. Zhang, F. Xi, S. Li, X. Wan, W. Ma, X. Chen, Z. Chen, R. Deng, J. Ji, H.-J. Fan, High-performance Si/nano-Cu/CNTs/C anode derived from photovoltaic silicon waste: A potential photovoltaic-energy storage strategy, Materials Today Energy, 20 (2021) 100671.

[3] T. Zhao, D. Zhu, W. Li, A. Li, J. Zhang, Novel design and synthesis of carbon-coated porous silicon particles as high-performance lithium-ion battery anodes, Journal of Power Sources, 439 (2019) 227027.

[4] F. Sun, Z. Hu, L. Wu, J. Chen, J. Luo, X. Wu, G. Cheng, R. Zheng, Reduced graphene oxide wrapped ultra-thin silicon nanowires for lithium ion battery anodes, Journal of Physics: Conference Series, IOP Publishing, 2020, pp. 012011.

[5] D. Liu, C. Chen, Y. Hu, J. Wu, D. Zheng, Z.-z. Xie, G. Wang, D. Qu, J. Li, D. Qu, Reduced graphene-oxide/highly ordered mesoporous SiOx hybrid material as an anode material for lithium ion batteries, Electrochimica Acta, 273 (2018) 26-33.

[6] X. Liu, J. Lu, J. Jiang, Y. Jiang, Y. Gao, W. Li, B. Zhao, J. Zhang, Enhancing lithium storage performance by strongly binding silicon nanoparticles sandwiching between spherical graphene, Applied Surface Science, 539 (2021) 148191.